

Detection of Close Kuiper Belt Binaries with HST WFC3

SIMON B. PORTER,¹ SUSAN D. BENECCHI,² ANNE J. VERBISCHER,³ W. M. GRUNDY,⁴ KEITH S. NOLL,⁵ AND
ALEX H. PARKER⁶

¹*Southwest Research Institute, 1050 Walnut St, Suite 300, Boulder, CO 80302, USA*

²*Planetary Science Institute, Tucson, AZ, USA*

³*University of Virginia, Charlottesville, VA, USA*

⁴*Lowell Observatory, Flagstaff, AZ, USA*

⁵*NASA Goddard Spaceflight Center, Greenbelt, MD, USA*

⁶*SETI Institute, Mountain View, CA, USA*

(Received 5/31/2023; Revised 4/2/2024; Accepted 4/14/2024)

Submitted to Planetary Science Journal

ABSTRACT

Binaries in the Kuiper Belt are common. Here we present our analysis of the Solar System Origins Legacy Survey (SSOLS) to show that using a PSF-fitting method can roughly double the number of binaries identified in that dataset. Out of 198 Kuiper Belt objects (KBOs) observed by SSOLS, we find 23 to be visually separated binaries, while a further 19 are blended-PSF binaries detectable with the method we present here. This is an overall binary fraction of 21% for the SSOLS dataset of cold classical KBOs. In addition, we tested our fitting methods on synthetic data, and while we were able to show it to be very effective at detecting certain blended-PSF binary KBOs, fainter or closer binary KBOs may easily be missed, suggesting that the close binary KBO fraction could be even higher. These results strongly support the idea that most (if not all) KBOs were formed through the Streaming Instability process, and as a consequence, most KBOs were formed as near-equal mass binaries.

Keywords: Classical Kuiper belt objects(250) — Trans-Neptunian objects(1705) — Asteroid satellites(2207)

1. INTRODUCTION

The Solar System is a highly evolved planetary system that betrays few clues of its origin, with the key exception of the Kuiper Belt. The present day Kuiper Belt consists almost exclusively of objects that formed outside of the giant planets and were either pushed outward by giant planet migration (the Neptune-resonant and scattered populations) or are still in the original orbits where they formed around the Sun (the classical KBOs; [McKinnon et al. 2020](#)). KBOs, and especially the cold classical KBOs (CCKBOs) which have the least perturbed heliocentric orbits, have suffered very little bombardment since their formation relative to asteroids interior of Jupiter ([Mao et al. 2021](#)), and no real thermal processing like comets ([Grundy et al. 2020](#)). The best constraints on the surfaces of KBOs come from the New Horizons mission, which flew past both the Pluto system and the CCKBO Arrokoth. Pluto itself is a highly-processed world with extensive surface-atmosphere interactions ([Stern et al. 2015](#)). Pluto’s large satellite Charon and two of four small satellites (Nix and Hydra) were imaged at sufficient resolution to show a small amount of cratering ([Robbins et al. 2017](#)), but since all the satellites were likely formed after a giant impact ([Canup 2011](#)), that says little about Kuiper Belt history as a whole. Arrokoth, a typical CCKBO ([Porter et al. 2018](#)), was much more constraining. It is constructed of two distinct lenticular lobes, connected on their equators, forming a contact binary ([Spencer et al. 2020](#)). There is a single large crater on the smaller lobe, and all other craters are significantly smaller ([Spencer et al. 2020](#)). This clean contact binary shape is unlike any object previously encountered by a spacecraft, but provides tantalizing clues to the formation processes of the solar system ([McKinnon et al. 2020](#)).

A leading theory of the formation of the Outer Solar System is the Streaming Instability (SI; [Nesvorný et al. 2019](#)). This postulates that solid bodies in the circumsolar disk initially formed when small clumps of solid material caused localized increases in gas drag, allowing the small clumps to very rapidly grow to full sized KBOs within tens of years ([Nesvorný et al. 2019](#), and citations therein). An important consequence of this rapid growth (when compared to more traditional slow accretion models) is that angular momentum grows rapidly too. SI thus tends to produce binary systems (and occasionally triple and higher systems), with most of the angular momentum in the mutual orbits ([Fraser et al. 2017](#)). In addition, because the source angular momentum is primarily from Keplerian shear, binaries produced by SI should be generally prograde ([Nesvorný et al. 2019](#)). And because SI requires the gas disk to happen, some fraction of SI-created binaries should have evolved inwards under gas drag until they became contact binaries (as may have happened for Arrokoth; [McKinnon et al. 2020](#)), while others evolved under mutual and solar tides to become tight circular binaries ([Porter & Grundy 2012](#)). SI thus predicts a Kuiper Belt filled with binaries of varying mutual separations, primarily prograde orbits, as well as a significant fraction of contact binaries.

The Kuiper Belt actually observed does indeed contain many binaries, which are primarily on prograde orbits ([Grundy et al. 2019](#)). Photometric lightcurve studies appear to show that at least 15% of CCKBOs are contact binaries ([Thirouin & Sheppard 2019](#)), though this number could be an underestimate due the difficulty of detecting contact binaries from lightcurves ([Showalter et al. 2021](#)). Similar studies of the (closer and brighter) 3:2 Neptune resonant “Plutinos” found a contact binary fraction of up to 50% ([Thirouin & Sheppard 2018](#)). Arrokoth is particularly instructive, as its dual-lenticular contact binary shape is best explained by formation as a binary by SI and slow evolution to contact under gas drag ([McKinnon et al. 2020](#)). The case for SI to be the leading formation mechanism for the Kuiper Belt, and the Outer Solar System generally, is thus very strong. However, a key prediction of SI is there should be a very large number of very tight (<3000 km separation) binary KBOs. The overall fraction of KBOs represented by these tight binaries is unknown, but must be significant to hide a large fraction of SI-produced binaries below the angular resolution of HST and ground-based adaptive optics systems. Measuring the separations of very tight binary KBOs (and especially CCKBOs) thus provides critical constraints not only on the SI, but on the processes that have sculpted the orbits of binary KBOs since then, including solar perturbations ([Porter & Grundy 2012](#)) and gas drag ([McKinnon et al. 2020](#)).

The Wide Field Camera 3 (WFC3) on the Hubble Space Telescope (HST) offers the best available tool to detect binary KBOs, as it is able to observe very faint objects with very high angular precision. Here we show we can detect and characterize binaries that are so close that they not clearly separated in HST/WFC3 images. This is aided by the fact that the WFC3 point spread function (PSF) is on average consistent and very well characterized, allowing for a precise measurement of a binary KBO with a separation of at least 0.5 pixels, as and bright as $V=24$. We apply this method to 198 CCKBOs observed with HST program GO-15648 (the Solar System Origins Legacy Survey, SSOLS), and show that it can roughly double the yield of binaries relative to those which can be easily detected with visual inspection. We also use this model to create 1000 synthetic KBO cases implanted in real HST images, and show the limits of this detection method.

2. TARGET SELECTION AND HST IMAGING

The Cycle 26 Treasury Program ‘The Solar System Origins Legacy Survey’ (SSOLS) observed 198 CCKBOs at optical wavelengths. This sample drew on three successful ground-based discovery surveys, the Deep Ecliptic Survey (DES; [Elliot et al. 2005](#)), the Canada France Ecliptic Plane Survey (CFEPS; [Petit et al. 2011](#)), and the Outer Solar System Origins Survey (OSSOS; [Bannister et al. 2018](#)). The DES was the first deep systematic survey to probe the population of the Kuiper Belt, and discovered 320 KBOs and Centaurs, including 43 of the SSOLS targets ([Elliot et al. 2005](#)). CFEPS probed 321 degree² of the sky, discovering and characterizing 169 KBOs, discovering 4 of the SSOLS targets ([Petit et al. 2011](#)). OSSOS was a followup of CFEPS, discovering over 800 KBOs and Centaurs, including 151 of the SSOLS targets ([Bannister et al. 2018](#)). The SSOLS targets were chosen to be cold classical KBOs that did not appear to be binary in the ground-based imagery, with the exception of 2005 EO₃₀₄, the widest binary in the SSOLS target list. This sample set of CCKBOs was designed to provide identifiable CCKBO binaries at a level that allows discovery bias to be quantified and removed, to better understand the binarity and luminosity function of the intrinsic CCKBO population. All of the targets (listed in Table 1) had well-determined orbits with at least three oppositions of data, to allow confidence in both their dynamical classification and that would be observable by the Hubble Space Telescope (HST) with a small subarray.

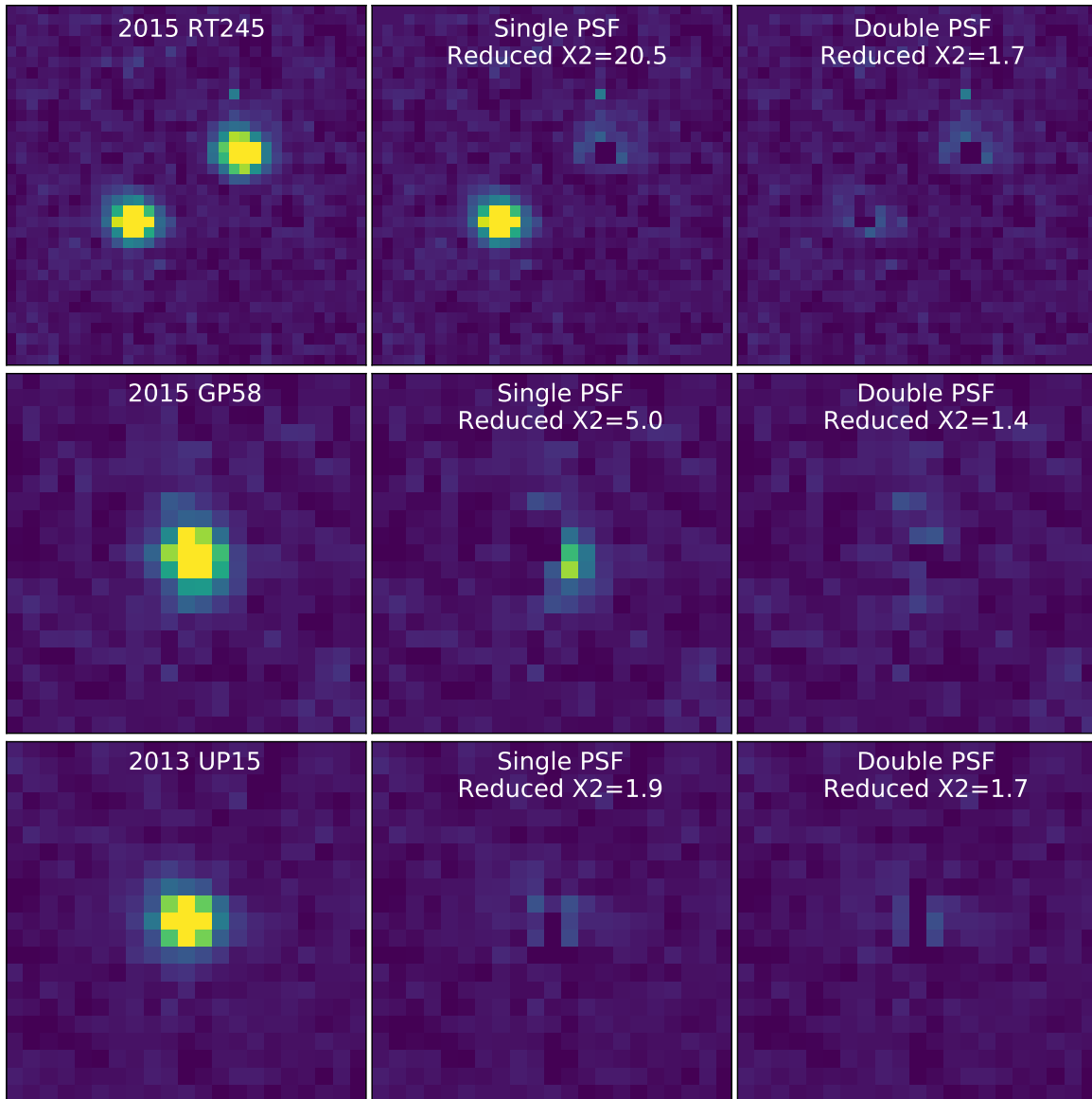


Figure 1. Examples of (top) a well-separated binary KBO, (middle) a blended binary KBO, and (bottom) a KBO that appears to be single. The top separated binary case accounted for 11.6% of the KBOs in the SSOLS dataset. For the middle case, the single-PSF solution only subtracts the primary, leaving behind a significant residual which is not there for the double-PSF solution, strongly indicating that this KBO is a blended binary. The residuals for the bottom case are almost identical for the single-PSF and double-PSF solutions, indicating that it is not binary to the resolution of HST/WFC3. All of these images are the F606W stacks for these objects; we performed the same analysis for the F814W stacks and enforced consistency between them for objects that we identified as blended binaries.

The 198 KBOs were successfully observed with HST program GO-15648, ranging in approximate apparent magnitude from $V=21$ to $V=25$. Observations of an additional 14 objects were attempted, but failed due to HST not correctly locking on to its guide star, leaving the observations unusable. The target CCKBOs were between 35.98 and 53.43 astronomical units from Earth at the time they were imaged, corresponding to a spatial resolution in the WFC3 images of 1044 to 1550 km/pixel. Each target KBO was observed with a single orbit, with four images in the F606W filter (roughly V-band), and four images in the F814W filter (roughly R-band), all using the UVIS2-C512C-SUB subframe. A four-point box dither was used for each filter. These filters were chosen to provide the most amount of color information while still maximizing the signal-to-noise ratio (SNR) for binary detection. F606W and F814W have also been used for previous HST observations of CCKBOs, particularly in support of the New Horizons mission (Benecchi

et al. 2019), allowing these observations to place both the color distribution of the binaries in context of the broader cold classical Kuiper Belt and the well-characterized New Horizons Distant KBO subset. Here we only present the results of relative astrometry and binary identification, while a following paper (in prep) will present the color results. An additional paper (in prep) will use these binaries to present a model for the size frequency distribution of binaries in the CCKBOs.

All of the data presented in this paper were obtained from the Mikulski Archive for Space Telescopes (MAST) at the Space Telescope Science Institute. The specific observations analyzed can be accessed via [doi:10.17909/6xbd-kd20](https://doi.org/10.17909/6xbd-kd20).

Table 1. The SSOLS target CCKBOs, their F606W magnitudes, their combined relative probabilities of being binary (Equation 5), the best-fit separation of the double-PSF case, the best-fit flux ratio of the the double-PSF case, and our judgement if the object is a separated binary, blended binary, or single.

		F606W Mag	Bin. Prob.	Pix. Sep.	Flux Ratio	Binary?
(612087)	1999 CU ₁₅₃	23.4	0.891	1.0	2.0:1	
(439858)	1999 ON ₄	23.6	0.425	1.1	2.5:1	
(612157)	2000 FG ₈	24.1	0.634	0.9	2.8:1	
(455206)	2001 FE ₁₉₃	23.0	0.082	1.5	5.7:1	
(612213)	2001 FK ₁₈₅	23.3	0.022	2.1	15.2:1	
(385362)	2002 PT ₁₇₀	23.3	0.014	2.7	9.0:1	
(469509)	2003 HC ₅₇	22.2	1.000	1.5	1.9:1	Blended
(612549)	2003 HG ₅₇	22.8	1.000	7.6	1.5:1	Separated
(363401)	2003 LB ₇	22.6	0.007	1.9	100.0:1	
(612619)	2003 SN ₃₁₇	22.9	0.998	0.8	2.0:1	Blended
	2003 UK ₂₉₃	23.4	0.186	1.2	10.2:1	
	2003 UV ₂₉₁	24.0	0.006	1.8	100.0:1	
(612733)	2003 YU ₁₇₉	23.0	1.000	1.1	1.7:1	Blended
(444018)	2004 EU ₉₅	23.0	0.001	6.2	100.0:1	
	2004 HD ₇₉	22.5	1.000	2.1	1.4:1	Separated
	2004 HE ₇₉	23.5	0.717	0.9	2.5:1	
(469610)	2004 HF ₇₉	22.9	1.000	3.2	1.4:1	Separated
	2004 HG ₇₉	23.1	0.629	1.0	2.6:1	
(444025)	2004 HJ ₇₉	23.3	0.958	1.3	2.6:1	Blended
	2004 HK ₇₉	23.4	1.000	3.1	1.1:1	Separated
	2004 KE ₁₉	22.7	1.000	3.3	2.2:1	Separated
	2004 KF ₁₉	22.7	0.043	4.1	54.2:1	
	2004 KG ₁₉	23.3	0.841	0.8	2.4:1	
	2004 MU ₈	23.0	1.000	4.3	1.3:1	Separated
	2004 PT ₁₁₇	23.1	0.984	1.0	2.3:1	Blended
	2004 PU ₁₁₇	23.2	0.089	1.1	6.6:1	
	2004 PV ₁₁₇	22.8	1.000	5.8	5.6:1	Separated
	2004 PW ₁₁₇	23.3	1.000	17.5	2.0:1	Separated
	2004 PX ₁₁₇	23.5	1.000	4.4	1.5:1	Separated
(609222)	2004 VB ₁₃₁	22.9	0.903	0.9	2.4:1	

Table 1 continued on next page

Table 1 (*continued*)

		F606W Mag	Bin. Prob.	Pix. Sep.	Flux Ratio	Binary?
(609221)	2004 VC ₁₃₁	22.0	0.294	1.3	2.2:1	
	2004 VD ₁₃₁	23.0	0.974	0.8	1.5:1	Blended
	2005 BW ₄₉	22.8	1.000	2.4	1.7:1	Separated
	2005 CE ₈₁	23.8	1.000	6.1	1.1:1	Separated
(525461)	2005 EN ₃₀₂	23.7	0.001	5.4	100.0:1	
(525462)	2005 EO ₃₀₄	22.6	1.000	43.1	4.2:1	Separated
	2006 CH ₆₉	23.2	1.000	23.0	1.7:1	Separated
	2006 JV ₅₈	23.3	1.000	3.6	1.7:1	Separated
	2006 QA ₁₈₁	23.5	0.010	3.0	9.9:1	
(587670)	2006 QE ₁₈₁	23.8	0.658	0.6	1.7:1	
	2006 QF ₁₈₁	23.4	0.999	0.8	1.6:1	Blended
(523615)	2006 UO ₃₂₁	23.7	0.088	1.4	9.4:1	
	2006 WF ₂₀₆	23.1	1.000	1.3	1.3:1	Blended
	2007 CQ ₇₉	23.4	0.884	1.1	3.6:1	
	2007 CS ₇₉	23.3	0.466	0.9	2.8:1	
	2007 DS ₁₀₁	22.8	1.000	2.1	1.3:1	Separated
	2013 EM ₁₄₉	23.0	1.000	1.3	2.0:1	Blended
(500840)	2013 GA ₁₃₈	23.9	0.483	0.7	1.4:1	
	2013 GB ₁₃₈	23.6	0.459	0.9	4.0:1	
	2013 GC ₁₃₈	23.6	0.219	1.9	12.4:1	
	2013 GD ₁₃₈	24.3	0.024	2.1	5.5:1	
	2013 GE ₁₃₈	24.3	0.053	1.5	5.9:1	
	2013 GF ₁₃₈	23.5	0.894	1.1	3.7:1	
(500835)	2013 GN ₁₃₇	22.9	0.997	1.2	2.5:1	Blended
	2013 GP ₁₃₇	23.8	0.005	1.7	100.0:1	
(500836)	2013 GQ ₁₃₇	23.5	0.076	1.5	5.9:1	
	2013 GR ₁₃₇	24.2	0.284	0.6	3.2:1	
	2013 GS ₁₃₇	23.9	0.317	0.9	3.1:1	
(500837)	2013 GT ₁₃₇	24.0	0.369	1.0	6.2:1	
	2013 GU ₁₃₇	23.7	0.668	0.7	1.5:1	
(500838)	2013 GV ₁₃₇	23.3	0.920	0.7	2.0:1	
(500839)	2013 GW ₁₃₇	23.8	0.070	1.6	4.5:1	
	2013 GX ₁₃₇	23.5	0.586	0.9	2.6:1	
	2013 GY ₁₃₇	23.7	0.130	0.8	2.5:1	
(500856)	2013 HT ₁₅₆	24.7	0.009	4.7	6.4:1	
	2013 SC ₁₀₁	24.1	0.036	0.9	100.0:1	
	2013 SD ₁₀₁	23.8	0.039	1.7	6.3:1	
	2013 SE ₁₀₁	24.1	0.340	1.0	2.8:1	
	2013 SF ₁₀₁	23.9	0.046	1.5	3.8:1	
	2013 SG ₁₀₁	24.5	0.042	2.4	11.4:1	
	2013 SJ ₁₀₀	24.5	0.628	0.9	6.8:1	

Table 1 *continued on next page*

Table 1 (*continued*)

	F606W Mag	Bin. Prob.	Pix. Sep.	Flux Ratio	Binary?	
	2013 SL ₁₀₀	23.8	0.854	0.9	2.2:1	
	2013 SO ₁₀₀	24.1	0.073	2.1	12.6:1	
(505446)	2013 SP ₉₉	23.4	0.578	0.8	2.3:1	
(505447)	2013 SQ ₉₉	23.4	1.000	3.4	1.5:1	Separated
	2013 SV ₁₀₀	23.9	0.766	0.8	2.3:1	
	2013 SX ₁₀₀	24.2	0.028	2.3	4.2:1	
	2013 UB ₁₈	24.2	0.076	2.2	6.5:1	
	2013 UC ₁₈	24.5	0.040	1.8	3.3:1	
	2013 UD ₁₈	23.7	0.005	1.8	100.0:1	
	2013 UG ₁₈	24.3	0.090	0.5	5.3:1	
(505476)	2013 UL ₁₅	23.2	1.000	4.3	1.6:1	Separated
	2013 UL ₁₇	24.4	0.001	5.9	100.0:1	
	2013 UN ₁₅	23.8	0.712	0.6	2.2:1	
	2013 UN ₁₇	24.4	0.116	1.0	6.5:1	
	2013 UO ₁₅	23.3	0.796	0.7	1.8:1	
	2013 UP ₁₅	23.6	0.842	0.6	2.1:1	
	2013 UP ₁₇	24.3	0.137	0.8	2.2:1	
	2013 UR ₁₇	24.1	0.917	0.6	1.9:1	
	2013 UT ₁₇	24.0	0.337	0.8	5.0:1	
	2013 UW ₁₆	23.6	0.970	1.1	1.4:1	Blended
	2013 UW ₁₇	24.3	0.325	0.9	5.2:1	
	2013 UY ₁₆	24.1	0.664	0.8	2.8:1	
	2013 UY ₁₇	23.8	0.022	2.4	4.0:1	
	2014 UC ₂₂₈	24.2	0.394	1.3	1.6:1	
	2014 UC ₂₂₉	24.7	0.436	0.8	3.6:1	
	2014 UC ₂₃₀	24.5	0.129	1.7	8.9:1	
(511551)	2014 UD ₂₂₅	23.1	0.984	0.9	2.1:1	Blended
(511552)	2014 UE ₂₂₅	22.7	0.768	0.5	1.4:1	
	2014 UL ₂₂₈	24.0	0.113	1.0	4.1:1	
	2014 UL ₂₂₉	24.3	0.003	6.0	17.3:1	
	2014 UP ₂₂₈	24.0	0.009	3.3	10.7:1	
	2014 UY ₂₂₈	24.2	0.033	2.0	4.0:1	
(523756)	2014 WD ₅₀₉	22.5	1.000	6.4	2.0:1	Separated
	2015 GA ₅₇	24.2	0.121	3.5	30.7:1	
	2015 GB ₅₇	24.5	0.107	0.9	3.6:1	
	2015 GC ₅₇	24.0	0.480	1.2	2.7:1	
	2015 GC ₅₈	24.3	0.962	0.8	5.1:1	Blended
	2015 GD ₅₇	23.8	0.022	0.8	100.0:1	
	2015 GD ₅₉	24.2	0.048	0.6	19.4:1	
	2015 GE ₅₇	24.5	0.006	1.7	100.0:1	
	2015 GF ₅₆	24.3	0.018	1.9	12.3:1	

Table 1 *continued on next page*

Table 1 (*continued*)

	F606W Mag	Bin. Prob.	Pix. Sep.	Flux Ratio	Binary?
2015 GF ₅₈	23.6	0.034	2.0	10.1:1	
2015 GF ₅₉	24.1	0.355	1.6	4.7:1	
2015 GG ₅₇	24.6	0.464	0.9	2.5:1	
2015 GH ₅₈	23.8	0.992	1.5	9.7:1	Blended
2015 GJ ₅₇	24.2	0.013	2.7	13.0:1	
2015 GK ₅₈	24.6	0.383	1.1	4.9:1	
2015 GL ₅₇	24.3	0.135	2.2	7.6:1	
2015 GL ₅₈	24.3	0.036	2.1	4.7:1	
2015 GM ₅₈	24.0	0.327	1.1	4.1:1	
2015 GN ₅₈	24.3	0.154	2.3	9.4:1	
2015 GO ₅₇	24.3	0.563	0.8	3.1:1	
2015 GO ₅₈	24.6	0.452	1.2	2.5:1	
2015 GP ₅₈	24.0	0.979	1.1	1.3:1	Blended
2015 GR ₅₆	24.1	0.596	0.8	3.4:1	
2015 GR ₅₇	24.0	0.008	3.3	12.3:1	
2015 GS ₅₆	24.5	0.853	1.0	1.9:1	
2015 GS ₅₇	24.0	0.150	1.1	3.2:1	
2015 GT ₅₈	24.4	0.204	1.4	3.1:1	
2015 GU ₅₆	23.5	0.952	0.8	1.7:1	Blended
2015 GU ₅₇	23.9	0.006	1.6	100.0:1	
2015 GU ₅₈	23.4	0.102	1.4	8.3:1	
2015 GW ₅₆	24.4	0.037	1.4	6.5:1	
2015 GW ₅₇	24.5	0.011	6.3	100.0:1	
2015 GX ₅₆	24.3	0.152	2.0	7.7:1	
2015 GY ₅₆	24.6	0.344	0.9	5.9:1	
2015 GY ₅₇	24.6	0.102	1.8	6.8:1	
2015 GZ ₅₆	23.5	0.007	6.6	100.0:1	
2015 GZ ₅₇	24.6	0.018	0.5	100.0:1	
2015 RA ₂₈₀	25.1	0.525	0.8	3.0:1	
2015 RB ₂₈₀	24.3	1.000	5.6	1.7:1	Separated
2015 RB ₂₈₁	23.5	0.029	1.8	12.0:1	
2015 RC ₂₈₁	24.1	0.026	1.9	7.4:1	
2015 RD ₂₈₀	24.4	0.015	0.9	100.0:1	
2015 RE ₂₈₀	24.6	0.025	2.4	4.5:1	
2015 RJ ₂₇₇	23.1	1.000	1.2	2.7:1	Blended
2015 RO ₂₈₁	23.0	1.000	1.2	6.2:1	Blended
2015 RP ₂₇₉	24.5	0.040	1.6	8.4:1	
2015 RP ₂₈₀	24.0	1.000	3.9	1.8:1	Separated
2015 RP ₂₈₁	25.2	0.439	0.5	1.4:1	
2015 RT ₂₄₅	23.6	1.000	12.2	1.1:1	Separated
2015 RZ ₂₇₉	24.2	0.017	3.2	5.0:1	

Table 1 *continued on next page*

Table 1 (*continued*)

	F606W Mag	Bin. Prob.	Pix. Sep.	Flux Ratio	Binary?
2015 VA ₁₆₉	24.3	0.715	1.1	3.2:1	
2015 VA ₁₇₂	23.6	0.045	2.0	10.9:1	
2015 VB ₁₆₉	24.6	0.001	6.1	100.0:1	
2015 VB ₁₇₀	23.7	0.874	1.0	2.3:1	
2015 VB ₁₇₁	24.6	0.164	1.1	4.1:1	
2015 VB ₁₇₃	24.3	0.005	1.6	100.0:1	
2015 VC ₁₇₀	23.6	0.286	0.8	4.5:1	
2015 VC ₁₇₂	23.8	0.003	6.2	100.0:1	
2015 VD ₁₆₉	24.1	0.005	1.7	100.0:1	
2015 VE ₁₆₉	24.0	0.019	2.3	6.1:1	
2015 VF ₁₆₉	24.5	0.036	1.7	3.4:1	
2015 VG ₁₆₉	24.7	0.040	1.4	7.0:1	
2015 VH ₁₆₉	25.2	0.003	6.9	58.1:1	
2015 VH ₁₇₁	23.7	0.143	1.1	4.4:1	
2015 VH ₁₇₃	23.8	0.024	1.6	7.6:1	
2015 VJ ₁₇₀	24.7	0.001	6.0	100.0:1	
2015 VK ₁₆₉	24.9	0.032	0.4	100.0:1	
2015 VK ₁₇₀	24.0	0.023	2.2	6.8:1	
2015 VL ₁₇₁	24.5	0.014	0.6	100.0:1	
2015 VM ₁₇₃	23.2	1.000	4.0	1.3:1	Separated
2015 VN ₁₇₁	24.3	0.003	5.9	10.9:1	
2015 VN ₁₇₂	24.3	0.265	0.9	2.8:1	
2015 VO ₁₇₁	24.1	0.269	1.0	4.2:1	
2015 VP ₁₆₈	24.4	0.547	0.8	1.8:1	
2015 VP ₁₇₂	24.4	0.100	1.1	5.7:1	
2015 VP ₁₇₃	24.3	0.012	3.7	9.2:1	
2015 VQ ₁₆₈	24.4	0.002	4.6	100.0:1	
2015 VQ ₁₆₉	23.9	0.712	0.8	2.6:1	
2015 VQ ₁₇₂	23.6	0.121	1.8	9.1:1	
2015 VQ ₁₇₃	23.7	0.824	1.0	2.8:1	
2015 VR ₁₆₈	24.5	0.289	1.2	4.5:1	
2015 VR ₁₇₂	23.6	0.315	1.0	8.6:1	
2015 VS ₁₆₈	24.3	0.008	3.7	6.2:1	
2015 VS ₁₇₂	24.3	0.232	0.8	2.0:1	
2015 VT ₁₆₈	22.9	0.997	0.9	3.4:1	Blended
2015 VU ₁₆₈	24.1	0.008	5.5	17.2:1	
2015 VU ₁₆₉	23.8	0.064	1.6	7.6:1	
2015 VU ₁₇₁	24.0	0.006	1.9	100.0:1	
2015 VW ₁₆₈	24.7	1.000	4.8	1.8:1	Separated
2015 VW ₁₇₀	24.4	0.005	9.7	5.0:1	
2015 VW ₁₇₂	24.8	0.362	1.6	6.5:1	

Table 1 *continued on next page*

Table 1 (*continued*)

	F606W Mag	Bin. Prob.	Pix. Sep.	Flux Ratio	Binary?
2015 VX ₁₆₉	24.2	0.088	1.5	5.0:1	
2015 VY ₁₇₀	23.9	0.724	0.9	2.0:1	
2015 VY ₁₇₂	24.1	0.069	1.6	8.1:1	
2015 VZ ₁₆₉	24.6	0.051	1.6	4.4:1	

3. IMAGE ANALYSIS

The first step in our image analysis was to reproject all of the images, in both filters, on to a common frame that cancelled out the dither pattern. Pixels affected by saturation, crosstalk, or CTE tails (as identified in the data quality part of the FLC files) were masked out here and in subsequent analysis. For most orbits, a 300x300 pixel initial image was sufficient to find the KBO, but a few required a 700x700 pixel window (i.e. the full frame with ample margin for dither). We then manually selected the object from this stacked image and recorded the offset to allow subsequent images to be properly centered. We next used the offsets to reproject the images again now centered on the objects with a smaller (181 pixel) window, upsampled from the original image by a factor of two. These second stacks were used to check if the object was a well-separated binary, as was the case for 23 of 198 KBOs. In the case that it was a separated binary, we recorded the positions of the assumed primary and secondary objects, and if no secondary was obvious, just the primary object. We then produced the final reprojected images, centered on the midpoint between the objects if a secondary was manually identified, or on the primary object if not. These final images were separately stacked for each of the two filters, F606W and F814W.

We then fit the separate stacks for each filter with a model Point Spread Function (PSF) from the Tiny Tim package (Krist 1995). We independently fit both of the filters with both a single-PSF and double-PSF model, and compared the resulting χ^2 . The image χ^2 was estimated as the sum of the square of the difference between the model and the stack of images. For the single-PSF cases, we used the manual pick of the primary as the initial location for the PSF, and then optimized the flux and x/y offset of the model PSF to minimise the image χ^2 . If the object had been manually identified as a binary in the prior steps, that was used as the initial conditions for the location of the secondary for the double-PSF cases. If there were not an identified secondary object, we used an initial guess of the brightest pixel of the residuals from the single-PSF fit.

If the double-PSF model showed little improvement over the single-PSF model, the two were held as equally likely, while if the double-PSF model was a significant improvement over the single-PSF model, we considered that to be likely a binary. We quantified this as:

$$\Delta_{prob} = \exp(-0.5 \times (\chi_{double}^2 - \chi_{single}^2)) \quad (1)$$

$$rprob_1 = \Delta_{prob} / (\Delta_{prob} + 1.) \quad (2)$$

Where Δ_{prob} is the relative likelihood of the double-PSF solution versus the single-PSF solution, and $rprob_1$ is the likelihood that the KBO is a binary based on the χ^2 residuals. If χ_{double}^2 is almost the same as χ_{single}^2 , then Δ_{prob} is close to unity, and $rprob_1$ is close to 0.5, as there is little evidence that either solution is superior. However, if χ_{double}^2 is much smaller than χ_{single}^2 , then Δ_{prob} is much larger than unity, and $rprob_1$ closer to 1.0, as there is strong evidence that the double-PSF solution is superior.

While this comparison of the χ^2 values is useful for filtering out the cases that were not improved with the double-PSF model, it is susceptible to low signal-to-noise ratio cases where the second PSF is fitting a coherent noise spike. We addressed this by fitting both filters independently, and then comparing the results for consistency. We dewighted the probability of being a binary for any case where the location of the secondary was larger than 1/4 pixel between the filters, or where the difference in the primary and secondary delta magnitudes was more than 1. The quarter-pixel test was based on a few tests with both real and synthetic data. We quantified this as:

$$rprob_2 = 0.25/|pixsep_{F606W} - pixsep_{F814W}| \quad (3)$$

$$rprob_3 = 1.0/|\Delta mag_{F606W} - \Delta mag_{F814W}| \quad (4)$$

$$rprob_{total} = rprob_1 \times rprob_2 \times rprob_3 \quad (5)$$

Where $pixsep_{F606W}$ and $pixsep_{F814W}$ are the primary-secondary separation distance in pixels for each of the two filters, Δmag_{F606W} and Δmag_{F814W} are the primary-secondary differences in magnitude for the two filters, and $rprob_{total}$ is the combined estimated probability of the KBO being binary. The constraint for Δmag consistency is weaker than for $pixsep$ to allow for the secondaries to have different F606W-F814W colors than primaries, but still useful to filter out inconsistent solutions.

4. CALIBRATION OF DETECTION EFFICIENCY

We sought to calibrate the detection efficiency of very close binary KBOs (and very close binary minor planets in general) with a set of simulations using the same fitting techniques as described above on synthetic data. Specifically, we selected four orbits from the SSOLS dataset (idy601, idy62h, idy64j, and idy693) that had a corner that was clear of stars and any diffraction spikes from the target KBO. For each of these four datasets, we then generated 250 synthetic model binary KBOs and added them to the real data in the F606W band, so that each synthetic binary KBO had real read noise and cosmic rays. We varied brightnesses of the primaries of the binaries from $V=21$ to $V=26$, the separation of the binaries from 0 to 3 WFC3 pixels, and the flux ratio between primary and secondary objects was tested at 1:1, 2:1, 5:1, and 10:1. The model assumed 0.1 pixels $1-\sigma$ of jitter per exposure.

Our simulation results can be seen in Figure 3. Equal-brightness binaries (top left of Figure 3) with $V=21$ combined brightness (roughly 400 km diameter for both objects at 40 AU and 5% albedo, same for following estimates) can be easily detected at separations as close as a half WFC3 pixel (roughly 600 km at 40 AU). This drops off with brightness, with a full pixel of separation being needed at $V=22.5$ (≈ 200 km diameters, ≈ 1200 km separation), and effectively no equal-brightness blended binaries were detectable at a combined magnitude less than $V=24.5$ (roughly 80 km diameter for both objects). HST/WFC3 is thus able to probe to the Roche limit for equal-brightness binaries larger than roughly 400 km, but is ineffective at detecting equal-brightness binaries smaller than 80 km diameter at separations less than at least 90 radii apart. This is crucial to understanding the missing tight binary population, as (523764) 2014 WC₅₁₀ was observed by stellar occultation to have a separation of 349 km, <4 radii apart (Leiva et al. 2020), and 2011 JY₃₁ was observed by New Horizons to have a separation of 198 km, a few radii apart (Weaver et al. 2022). In addition, the simulations of Porter & Grundy (2012) showed there should be a large number of binary KBOs at separations of a few radii, as that is where tidal forces circularized orbits and stopped semimajor axis decay. HST/WFC3 is thus generally insensitive to a potentially large population of binary KBOs that is both known to exist from other detection methods, and predicted by theory.

Binary KBOs with a 2:1 brightness ratio fared only slightly worse, with a similar binary recovery rate for $V=21$ (primary roughly 500 km diameter, secondary roughly 300 km), down to half a pixel (roughly 600 km), and $V=22.5$ (primary roughly 240 km, secondary 170 km) also needing a full pixel of separation (1200 km). However, the drop to a 2:1 flux ratio increased the threshold of any blended binary detection at 3 pixels from $V=24.5$ to $V=24.0$ (120 and 85 km diameters). At 5:1 brightness ratio, the minimum combined brightness for the detection of a satellite was $V=23$ (primary diameter about 210 km, secondary 95 km). At 10:1 brightness ratio, the minimum combined brightness for the detection of a satellite was $V=21.5$ (primary diameter about 440 km, secondary 140 km).

5. RESULTS AND DISCUSSION

We have performed initial binary detection and for all the data in program GO-15648. The results of our analysis of binary probability are listed in Table 1, and compared to the known binary KBOs in Figure 2. Of the 198 objects that were successfully observed, we identified 23 as being visually separated binaries, a further 19 as blended binaries with a probability of being binary of being $>95\%$ (per the formulation above), and 156 that appeared as singular objects to our analysis. Our blended binary analysis was thus able to almost double the yield of binary KBOs in the SSOLS dataset.

Our detection of a large number of blended-PSF binary KBOs implies that binary KBOs at apparent separations at or just below the detection limit of HST/WFC3 may be very common. This argument is further strengthened by our

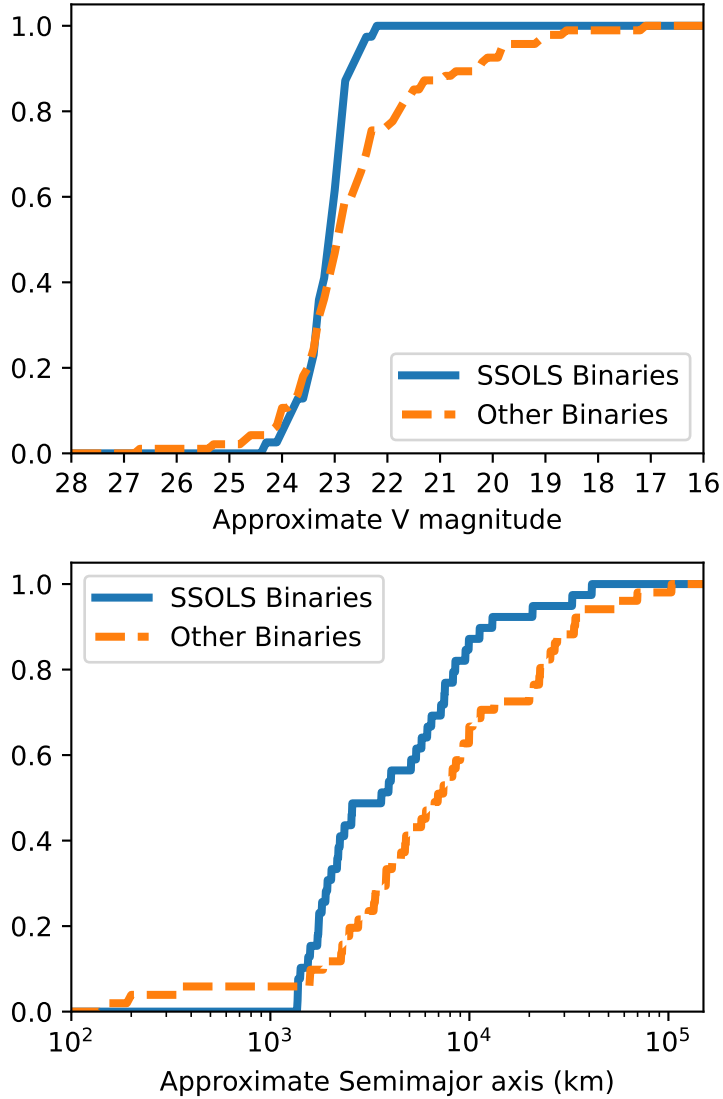


Figure 2. Cumulative distributions of the brightnesses and physical separations of the SSOLS binaries in Table 1 (blue, solid) in comparison with the known KBO binaries (orange, dashed) listed at <http://www2.lowell.edu/users/grundy/tnbs/status.html>. The semimajor axes of the SSOLS binaries is estimated as their apparent separation times $\sqrt{2}$. The SSOLS binaries are both fainter and tighter than the known binary KBOs. The only binary KBOs that are tighter than the SSOLS blended binaries are the two detected by New Horizons (2011 JY₃₁ and 2014 OS₃₉₃; Weaver et al. 2022) and the third by a stellar occultation (2014 WC₅₁₀; Leiva et al. 2020).

synthetic KBO analysis which shows that close binary KBOs dimmer than $V=24$ and with flux ratios larger than 5:1 are very hard for WFC3 to detect, even with apparent separations greater than one pixel. A full census of the binary fraction in the Kuiper Belt is thus very difficult from direct imaging alone. Ground-based adaptive optics systems are even more flux limited than HST (Grundy et al. 2011) and cannot probe binaries that are fainter or closer than those detectable with HST/WFC3. The James Webb Space Telescope (JWST) with the NIRC*am* instrument only offers a marginal increase in angular resolution over WFC3 (≈ 30 milliarcseconds/pixel versus ≈ 40 milliarcseconds/pixel for WFC3), but may be able to detect fainter KBO satellites due to its larger collecting area.

The strongest evidence that very tight binary KBOs may be common comes from two unconventional binary detection methods, a stellar occultation and direct spacecraft observations. The 3:2 Neptune resonant KBO (523764) 2014 WC₅₁₀ was observed by stellar occultation to have a separation of 349 km (Leiva et al. 2020), which corresponds to an apparent

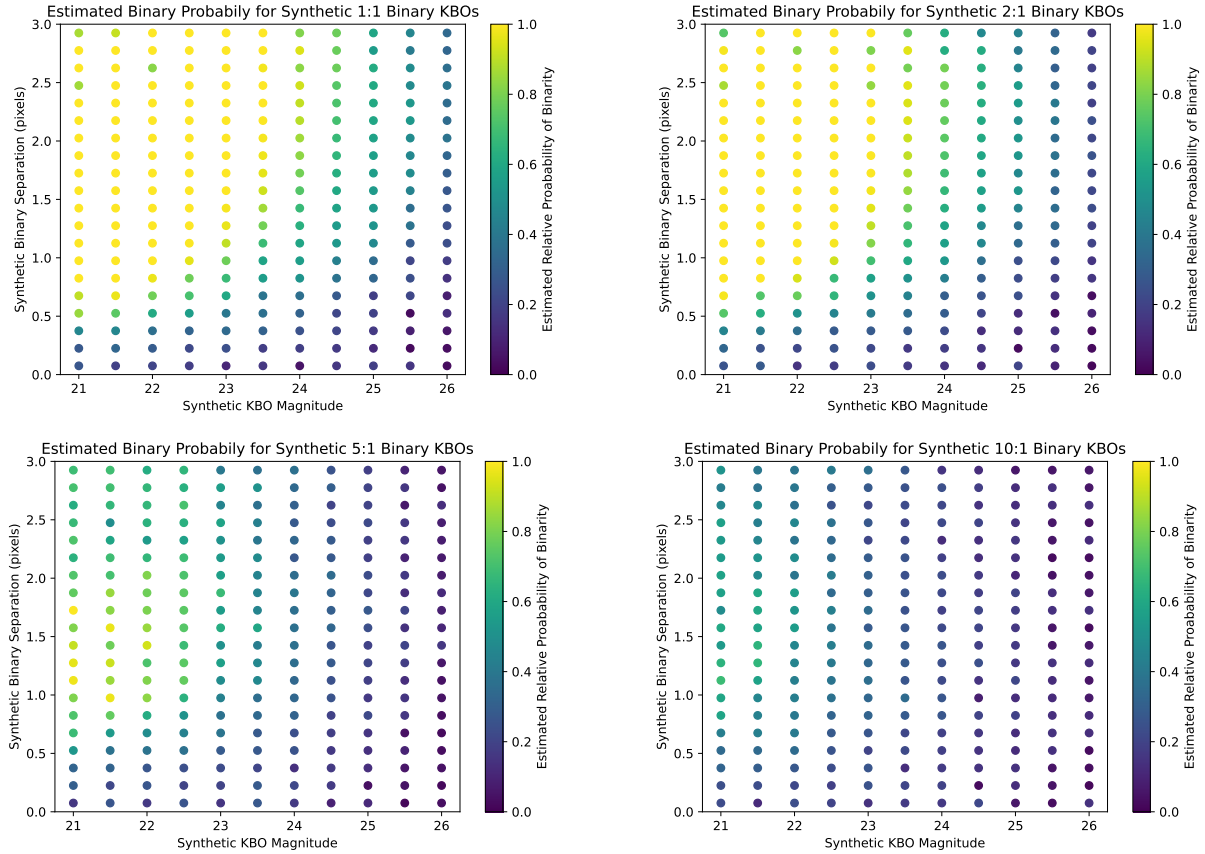


Figure 3. Recovery efficiency of simulated binary KBOs with SSOLS-style synthetic data, assuming jitter of 0.1 pixels and F606W-F814W color of 0.72. Each panel corresponds to 1000 simulations with a different primary/secondary flux ratio. The synthetic data was processed in the same way as the actual SSOLS data. The separations of the synthetic binaries were varied uniformly from 0 to 3 pixels, but binned and averaged here for clarity. Recovery efficiency was as expected better for brighter satellites farther away, with very few (but still some) 10:1 flux ratio binaries detectable. None of the synthetic single-PSF cases were detected as a false-positive binary at 95% confidence.

separation of 13 milliarcseconds, or less than a 1/3 of a WFC3 pixel. The New Horizons spacecraft observed five KBOs with the LORRI camera at a distance of less than 0.1 astronomical units, and two of them appeared to be very close binaries, 2011 JY₃₁ and 2014 OS₃₉₃ (Weaver et al. 2022). 2011 JY₃₁ was resolved as a blended binary in both LORRI epochs, and the combination of that with the assumption of the orbital period being equal to the lightcurve period of 46 hours allowed the mutual orbit separation to be fit as 199 km (Weaver et al. 2022). 2014 OS₃₉₃ was only observed to be binary in one of the two epochs, and Weaver et al. (2022) estimated its apparent separation to be ≈ 150 km. These separations would be < 0.2 WFC3 pixels as seen by HST, and sure enough, neither 2011 JY₃₁ nor 2014 OS₃₉₃ appears obviously binary in HST WFC3 imaging (Weaver et al. 2022). While these unconventional detections are hard to reproduce, they do strongly argue that binary KBOs with separations below the detection threshold of WFC3 should be common. These tight binaries may be a result of direct formation from the protoplanetary disk by the streaming instability (e.g. Fraser et al. 2017; Nesvorný et al. 2019), or the result of post-formation orbital evolution (e.g. Porter & Grundy 2012), or some combination of those processes. The discovery of both of these very tight binary KBOs (< 400 km) with unconventional methods, and the large number of 1000-3000 km binaries that we found in the SSOLS dataset, shows that there is likely to be a substantial number of Kuiper Belt binaries with 300-1000 km separations.

The inclinations of binary KBOs to their orbits has been shown to be very preferentially prograde (Grundy et al. 2019). This provides an important constraint on the formation of binary KBOs, as it strongly supports the formation of KBO binaries by SI (Nesvorný et al. 2019). However, this test has only been performed for relatively wide KBO binaries (Grundy et al. 2019), as very few tight binaries have fully determined orbits. Formation models (e.g. Nesvorný et al. 2019) show that most binary KBOs formed wider and more eccentric than the observed binary KBOs (Grundy

et al. 2019), before the mutual orbits evolved under perturbations to tighter, more circular orbits (Porter & Grundy 2012). Models imply that the prograde preference should be preserved under that mutual orbit evolution (Porter & Grundy 2012), but that has not yet been proven, and can only be tested by measuring the orbits of tight binary KBOs. Future observations of the blended binary KBOs discovered in this program could fit their mutual orbits which would be very useful to test if this prograde preference is indeed preserved to much tighter separations.

6. FUTURE OBSERVATIONS AND ANALYSIS

HST/WFC3 has historically been the high-resolution instrument available for this work (e.g. Grundy et al. 2019, and citations therein), but JWST/NIRCam does offer slightly higher resolution than WFC3 (Rieke et al. 2023), with a much larger collecting area. However, JWST observations of KBOs is challenging, as the design of the spacecraft prevents it from observing the Kuiper Belt except at the quadratures, and after the micrometeorite constraint imposed in Cycle 2, only the post-opposition quadrature window is available. Any KBO must therefore be observed by JWST within a narrow, roughly two week window, away from the opposition surge that pushes faint KBOs to their maximum brightness, and with slow moving background stars that may be confused for KBO satellites. In addition, the narrow observing window of quadrature-only space telescopes, like JWST and the Roman Space Telescope, makes recovery of the mutual orbits of binary KBOs effectively impossible, as they cannot cover the required temporal range (Grundy et al. 2008). The Keck laser adaptive optics system has been used extensively for recovery of binary KBOs at slightly lower resolution than HST (Grundy et al. 2011). Future ground-based facilities like the Extremely Large Telescope (ELT) and the Thirty Meter Telescope (TMT) may be able to directly resolve even tighter binaries, with their larger collecting areas being able to compensate for the throughput losses inherent in adaptive optics systems. In addition, both of those future large telescopes are planned to use multi-point laser adaptive optics systems (Diolaiti et al. 2016; Boyer et al. 2014) which would enable them to observe KBOs without the need of a stellar appulse for tip/tilt correction (as used by Keck), increasing their operational flexibility.

The most promising pathway to surveying the very close binary population of the Kuiper Belt may be through stellar occultations. As Leiva et al. (2020) has shown, stellar occultation can detect binary KBOs down to arbitrary separations, and the use of the Gaia DR3 star catalog (Gaia Collaboration et al. 2021) allows these occultations to be targeted with great precision (Porter et al. 2018). The advent of low cost cameras with GPS timing precision enables stellar occultations to be observed with small, highly mobile telescopes, greatly increasing the coverage possible for a given occultation event. Given that 2/6 KBOs observed up close by New Horizons (including Arrokoth) were apparently binaries with less than 200 km separation, it would not take many stellar occultations to find additional very close binary KBOs.

For future analysis of this and similar datasets, we plan to enhance binary detection with the use of Machine Learning (ML). The current results are based on shifting Tiny-Tim PSFs and assumptions about the noise properties of WFC3 images. To use ML, we would create a large amount of synthetic single and binary KBOs (much larger than used for our calibration here) and then train a neural network to distinguish between them. This could result in a much more effective detection of barely-resolvable binary KBOs, and would enable the application of this method to historical observations of KBOs by HST to find even more blended-PSF binaries.

7. CONCLUSIONS

We performed a PSF-fitting process on 198 KBOs observed with HST/WFC3 and found that while 11.6% appeared to be visually separated binaries, a further 9.6% were blended-PSF binaries. Our results show that binary KBOs at or below the detection threshold of HST appear to be at least as common as binary KBOs that appear to be well separated in WFC3/UVIS images. This was confirmed by our application of the same fitting method to synthetic data, which found that binary KBOs fainter than $V=24$ or with primary/secondary flux ratios larger than 5:1 are very unlikely to be detectable with HST. These results appear to support the idea that the Kuiper Belt was formed through the Streaming Instability process, and that most if not all KBOs were born as binary systems.

This work was supported by HST program GO-15648. HST data was obtained from the Space Telescope Science Institute, which is operated by the Association of Universities for Research in Astronomy, Inc., under NASA contract NAS 5-26555.

Software: Astropy (Astropy Collaboration et al. 2022), Scipy (Virtanen et al. 2020), Photutils (Bradley et al. 2022), Spiceypy (Annex et al. 2021), Tiny Tim (Krist 1995),

REFERENCES

- Annex, A., Pearson, B., Seignovert, B., et al. 2021, AndrewAnnex/Spiceypy: Spiceypy 4.0.1, v4.0.1, Zenodo, Zenodo, doi: [10.5281/zenodo.4883901](https://doi.org/10.5281/zenodo.4883901)
- Astropy Collaboration, Price-Whelan, A. M., Lim, P. L., et al. 2022, ApJ, 935, 167, doi: [10.3847/1538-4357/ac7c74](https://doi.org/10.3847/1538-4357/ac7c74)
- Bannister, M. T., Gladman, B. J., Kavelaars, J. J., et al. 2018, ApJS, 236, 18, doi: [10.3847/1538-4365/aab77a](https://doi.org/10.3847/1538-4365/aab77a)
- Benecchi, S. D., Borncamp, D., Parker, A. H., et al. 2019, Icarus, 334, 22, doi: [10.1016/j.icarus.2019.01.025](https://doi.org/10.1016/j.icarus.2019.01.025)
- Boyer, C., Adkins, S., Andersen, D. R., et al. 2014, in Society of Photo-Optical Instrumentation Engineers (SPIE) Conference Series, Vol. 9148, Adaptive Optics Systems IV, ed. E. Marchetti, L. M. Close, & J.-P. Vran, 91480X, doi: [10.1117/12.2056863](https://doi.org/10.1117/12.2056863)
- Bradley, L., Sipócz, B., Robitaille, T., et al. 2022, astropy/photutils: 1.5.0, 1.5.0, Zenodo, Zenodo, doi: [10.5281/zenodo.6825092](https://doi.org/10.5281/zenodo.6825092)
- Canup, R. M. 2011, AJ, 141, 35, doi: [10.1088/0004-6256/141/2/35](https://doi.org/10.1088/0004-6256/141/2/35)
- Diolaiti, E., Ciliegi, P., Abicca, R., et al. 2016, in Society of Photo-Optical Instrumentation Engineers (SPIE) Conference Series, Vol. 9909, Adaptive Optics Systems V, ed. E. Marchetti, L. M. Close, & J.-P. Véran, 99092D, doi: [10.1117/12.2234585](https://doi.org/10.1117/12.2234585)
- Elliot, J. L., Kern, S. D., Clancy, K. B., et al. 2005, AJ, 129, 1117, doi: [10.1086/427395](https://doi.org/10.1086/427395)
- Fraser, W. C., Bannister, M. T., Pike, R. E., et al. 2017, Nature Astronomy, 1, 0088, doi: [10.1038/s41550-017-0088](https://doi.org/10.1038/s41550-017-0088)
- Gaia Collaboration, Brown, A. G. A., Vallenari, A., et al. 2021, A&A, 649, A1, doi: [10.1051/0004-6361/202039657](https://doi.org/10.1051/0004-6361/202039657)
- Grundy, W. M., Noll, K. S., Virtanen, J., et al. 2008, Icarus, 197, 260, doi: [10.1016/j.icarus.2008.04.004](https://doi.org/10.1016/j.icarus.2008.04.004)
- Grundy, W. M., Noll, K. S., Nimmo, F., et al. 2011, Icarus, 213, 678, doi: [10.1016/j.icarus.2011.03.012](https://doi.org/10.1016/j.icarus.2011.03.012)
- Grundy, W. M., Noll, K. S., Roe, H. G., et al. 2019, Icarus, 334, 62, doi: [10.1016/j.icarus.2019.03.035](https://doi.org/10.1016/j.icarus.2019.03.035)
- Grundy, W. M., Bird, M. K., Britt, D. T., et al. 2020, Science, 367, aay3705, doi: [10.1126/science.aay3705](https://doi.org/10.1126/science.aay3705)
- Krist, J. 1995, in Astronomical Society of the Pacific Conference Series, Vol. 77, Astronomical Data Analysis Software and Systems IV, ed. R. A. Shaw, H. E. Payne, & J. J. E. Hayes, 349
- Leiva, R., Buie, M. W., Keller, J. M., et al. 2020, PSJ, 1, 48, doi: [10.3847/PSJ/abb23d](https://doi.org/10.3847/PSJ/abb23d)
- Mao, X., McKinnon, W. B., Singer, K. N., et al. 2021, Journal of Geophysical Research (Planets), 126, e06961, doi: [10.1029/2021JE006961](https://doi.org/10.1029/2021JE006961)
- McKinnon, W. B., Richardson, D. C., Marohnic, J. C., et al. 2020, Science, 367, aay6620, doi: [10.1126/science.aay6620](https://doi.org/10.1126/science.aay6620)
- Nesvorný, D., Li, R., Youdin, A. N., Simon, J. B., & Grundy, W. M. 2019, Nature Astronomy, 3, 808, doi: [10.1038/s41550-019-0806-z](https://doi.org/10.1038/s41550-019-0806-z)
- Petit, J. M., Kavelaars, J. J., Gladman, B. J., et al. 2011, AJ, 142, 131, doi: [10.1088/0004-6256/142/4/131](https://doi.org/10.1088/0004-6256/142/4/131)
- Porter, S. B., & Grundy, W. M. 2012, Icarus, 220, 947, doi: [10.1016/j.icarus.2012.06.034](https://doi.org/10.1016/j.icarus.2012.06.034)
- Porter, S. B., Buie, M. W., Parker, A. H., et al. 2018, AJ, 156, 20, doi: [10.3847/1538-3881/aac2e1](https://doi.org/10.3847/1538-3881/aac2e1)
- Rieke, M. J., Kelly, D. M., Misselt, K., et al. 2023, PASP, 135, 028001, doi: [10.1088/1538-3873/acac53](https://doi.org/10.1088/1538-3873/acac53)
- Robbins, S. J., Singer, K. N., Bray, V. J., et al. 2017, Icarus, 287, 187, doi: [10.1016/j.icarus.2016.09.027](https://doi.org/10.1016/j.icarus.2016.09.027)
- Showalter, M. R., Benecchi, S. D., Buie, M. W., et al. 2021, Icarus, 356, 114098, doi: [10.1016/j.icarus.2020.114098](https://doi.org/10.1016/j.icarus.2020.114098)
- Spencer, J. R., Stern, S. A., Moore, J. M., et al. 2020, Science, 367, aay3999, doi: [10.1126/science.aay3999](https://doi.org/10.1126/science.aay3999)
- Stern, S. A., Bagenal, F., Ennico, K., et al. 2015, Science, 350, aad1815, doi: [10.1126/science.aad1815](https://doi.org/10.1126/science.aad1815)
- Thirouin, A., & Sheppard, S. S. 2018, AJ, 155, 248, doi: [10.3847/1538-3881/aac0ff](https://doi.org/10.3847/1538-3881/aac0ff)
- . 2019, AJ, 157, 228, doi: [10.3847/1538-3881/ab18a9](https://doi.org/10.3847/1538-3881/ab18a9)
- Virtanen, P., Gommers, R., Oliphant, T. E., et al. 2020, Nature Methods, 17, 261, doi: [10.1038/s41592-019-0686-2](https://doi.org/10.1038/s41592-019-0686-2)
- Weaver, H. A., Porter, S. B., Spencer, J. R., & The New Horizons Science Team. 2022, PSJ, 3, 46, doi: [10.3847/PSJ/ac4cb7](https://doi.org/10.3847/PSJ/ac4cb7)